AGU PUBLICATIONS

JGR

Journal of Geophysical Research: Oceans

RESEARCH ARTICLE
10.1002/2017JC013310

Special Section:
Oceanic Responses and Feedbacks to Tropical Cyclones

Microseisms Generated by Super Typhoon Megi in the Western Pacific Ocean

Jianmin Lin[1], Jian Lin[2,3], and Min Xu[3]

[1]Marine Acoustics and Remote Sensing Laboratory, Zhejiang Ocean University, Zhoushan, China, [2]Department of Geology and Geophysics, Woods Hole Oceanographic Institution, Woods Hole, MA, USA, [3]CAS Key Laboratory of Ocean and Marginal Sea Geology, Chinese Academy of Sciences, South China Sea Institute of Oceanology, Guangzhou, China

Key Points:
- The coupled ocean and solid Earth responses to typhoon Megi were investigated by combined analysis and modeling of microseisms
- Microseisms were observed to be excited near coasts and also hypothesized to originate at the left-rear quadrant of the typhoon center
- Megi generated stronger microseisms when over the South China Sea shallow continental shelf than over the Philippine Sea deep basins

Correspondence to:
J. Lin,
jlin@whoi.edu;
M. Xu,
mxu@scsio.ac.cn

Citation:
Lin, J., Lin, J., & Xu, M. (2017). Microseisms generated by super typhoon Megi in the western Pacific Ocean. *Journal of Geophysical Research: Oceans*, *122*, 9518–9529. https://doi.org/10.1002/2017JC013310

Received 27 JUL 2017
Accepted 15 NOV 2017
Accepted article online 17 NOV 2017
Published online 7 DEC 2017

Abstract Microseisms generated by the super typhoon Megi (13–24 October 2010) were detected on both land-based and island-based seismic stations. We applied temporal frequency spectrum analysis to investigate the temporal evolution of the microseisms. When Megi was over the deep basins of the Philippine Sea, only weak microseisms with short-period double frequency (SPDF, ~0.20–0.40 Hz) were observed. However, after Megi traveled into the shallower waters of the South China Sea, microseisms with both long-period double frequency (LPDF, ~0.12–0.20 Hz) and SPDF were recorded. The excitation source regions of the microseisms were analyzed using seismic waveform records and synthetic modeling in frequency domain. Results reveal that part of the LPDF microseisms were excited in coastal source regions, while the intensity of both LPDF and SPDF microseisms correlated well with the distance from seismic stations to the typhoon center. Synthetic computations of equivalent surface pressure and corresponding microseisms show that the wave-to-wave interaction induced by coastal reflection has primary effects on microseismic frequency band of ~0.10–0.20 Hz. The coastal generation of the dispersive LPDF microseisms is also supported by the observation of ocean swells induced by Megi through the images of C-band ENVISAT-ASAR satellite during its migration process. Two source regions of the microseisms during the life span of Megi are finally distinguished: One was mainly located in the left-rear quadrant of the typhoon center that generated both LPDF and SPDF microseisms at shallow seas, while the other one was near the coasts that generated mostly LPDF microseisms.

1. Introduction

Microseisms are one of the most energetic components of seismic noise (Bromirski, 2001; Bromirski et al., 2005; Dorman et al., 1993; Friedrich et al., 1998; Haubrich & McCamy, 1969; Rhie & Romanowicz, 2004; Schulte-Pelkum et al., 2004; Sutton & Barstow, 1990). Ocean-surface agitation driven by wind and waves has long been accepted as a major source of microseisms on land and ambient noise in the ocean (Knudsen et al., 1948; Longuet-Higgins, 1950; Wenz, 1962). A portion of the energy inherited from the large and complex ocean waves at the sea surface, e.g., generated by typhoons, can propagate to the water-rock interface at the seafloor and be transferred into seismic waves in the basement rocks as "microseisms" (with frequency typically of 0.05–0.4 Hz). The microseisms can propagate as both surface waves (mainly Rayleigh-type) and compressional (P) waves (Gerstoft et al., 2006, 2008; Zhang et al., 2010) and be recorded worldwide by broadband seismometers.

Microseisms commonly exhibit two prominent peaks in the frequency spectra: single frequency (SF, typically 0.05–0.12 Hz) and double frequency (DF, typically 0.12–0.4 Hz), corresponding to two different generation processes. SF microseisms are generated by the ocean wave-induced pressure fluctuations on the shallow seafloor or the shore, thus having the same frequency range of the ocean waves (Hasselmann, 1963). Because the pressure induced by ocean waves decays exponentially with water depth with an e-folding constant equal to the wavenumber (Webb, 1998), source regions of SF microseisms are generally concentrated on coastal areas. DF microseisms are generated by the depth-independent pressure fluctuations on the seafloor induced by nonlinear interaction between ocean waves, which have nearly the same frequency and travel in opposite directions (Longuet-Higgins, 1950). Therefore, DF microseisms have twice the frequency of ocean waves, while their intensities depend on the amplitude of the opposing ocean waves and the area of the source region where the nonlinear interaction occurs. DF microseisms can be

further classified as long-period DF (LPDF, typically 0.12–0.2 Hz) and short-period DF (SPDF, typically 0.2–0.4 Hz) microseisms, generated by the relative long-period ocean swells and relatively short-period local sea winds, respectively (Bromirski et al., 2005).

Microseisms generated by typhoons have already been well detected and measured by broadband seismographs on terrestrial seismic stations (e.g., Chen et al., 2015; Gerstoft et al., 2006; Obrebski et al., 2012; Sufri et al., 2014; Sun et al., 2013) and ocean bottom seismometers (e.g., Chi et al., 2010; Davy et al., 2014; Lin et al., 2014). The source regions of DF microseisms have also been determined based on seismic data using different techniques, such as beamforming study (e.g., Landès et al., 2010), polarization analysis (e.g., Schimmel & Gallart, 2004), and numerical modeling (e.g., Gualtieri et al., 2014; Kedar et al., 2008). Ardhuin et al. (2011) presented the first numerical model of microseism generation by random ocean waves, and summarized three types of generation mechanism of DF microseisms from wave-to-wave interactions under typhoon conditions. However, because of the complexity and instability of the spectral characteristics of the ocean waves either in temporal or spatial domain, the identification of the source region and generation mechanism of DF microseisms are so far complicated and still under debate (Bromirski et al., 2013).

In this study, we investigated the microseisms generated by the 2010 super typhoon Megi, the largest typhoon recorded in recent history, over the western Pacific Ocean through both seismic observation and numerical modeling. The unusual size of Megi and its long track across the contrasting deeper and shallower basins of the Philippine Sea and South China Sea (SCS), respectively, provide an unprecedented opportunity to identify the complex distribution of the source regions and key factors affecting the characteristics of the microseisms. Two main source regions, around the typhoon center and near coasts, respectively, were distinguished for generating the DF microseisms during the life span of Megi. Ocean wave interactions around the left-rear quadrant of the typhoon center were found to have generated both the LPDF and SPDF microseisms, while interactions near the coasts mainly generated the LPDF microseisms. The observed temporal and spatial characteristics of the DF microseisms generated from source region around the typhoon center indicate that water depth has played an important role in the generation of the observed DF microseisms.

2. Data Analysis

Typhoon Megi of 2010, in the highest classification (Category 5) on the Saffir-Simpson scale, was one of the strongest typhoons recorded. According to the data of the Regional Specialized Meteorological Center (RSMC), Megi had achieved the highest 10 min maximum sustained wind speed (230 km/h) since typhoon Bess in 1982, and the lowest atmospheric pressure (885 hPa) since typhoon Vanessa in 1984. Megi formed on 13 October in the deep Philippine Sea and reached peak strength before making its first landfall over the Luzon Island on early 18 October (Figure 1). Weakened due to land interaction over the Luzon Island, Megi drifted into the SCS and turned northward to the Taiwan Strait. On 23 October, Megi made its second landfall in SE China and dissipated gradually afterward. The complicated track course of Megi over contrasting deeper and shallower ocean basins provides a great opportunity for comparison of microseisms generated under different conditions, allowing us to identify the possible source regions and investigate the generation mechanisms of microseisms.

Vertical component seismic waveform data recorded on a total of 154 seismic stations within ~1,500 km from the track line of Megi were obtained from the IRIS Data Management Center, China Earthquake Networks Center, and the F-net network of Japan (Figure 1). The data span the period of 10–25 October, including 3 days prior to the onset of Megi.

The seismic waveform records were analyzed to reveal the intensity of the microseisms as a function of time, space, and frequency. First, the seismic waveform data were preprocessed through (1) demeaning and detrending; (2) removal of instrument response; (3) resampling to 1 point per second; and (4) filtering with a band-pass filter of 0.05–0.45 Hz. Second, the temporal frequency spectrogram, calculated using the short-time Fourier transform with a moving time-window length of 2,048 points shifted in steps of 1,800 points (i.e., half an hour), was employed to study the time-frequency characteristics of the microseisms recorded on different seismic stations. Third, synthetic modeling was conducted to determine the excitation source regions. Finally, we utilized the ENVISAT-ASAR satellite image taken at 01:26 UTC on 17 October to

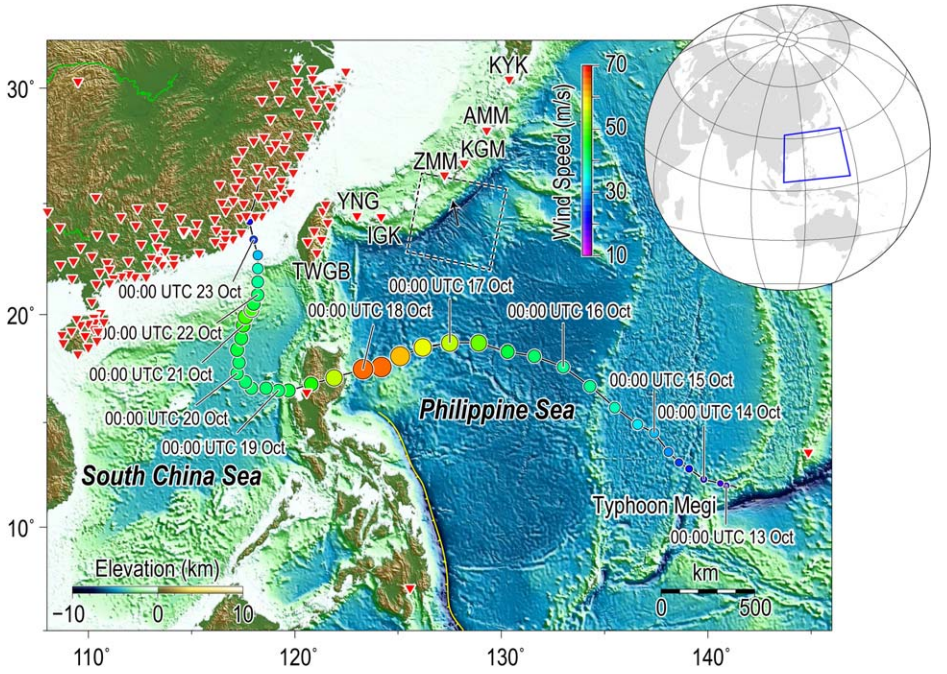

Figure 1. Distribution of seismic stations (red triangles) and track of typhoon Megi (colored circles) on top of shaded relief bathymetry of the Philippine Sea and South China Sea. The seismic stations are mostly from the China Digital Seismograph Network (CDSN), Broadband Array in Taiwan for Seismology (BATS), and F-net network in Japan. Location of station TWGB (example shown in Figure 2) and stations on the Ryukyu Islands are labeled. The typhoon track is indicated by rounded circles spaced in 6 h time intervals, with circle size proportional to wind speed, which is also represented by the color of the circle simultaneously. The best-track data of Megi are provided by the Japan Meteorological Agency (http://www.jma.go.jp/jma/jma-eng/jma-center/rsmc-hp-pub-eg/trackarchives.html). The dashed rectangular box and inserted black arrow represent the observation coverage of the C-band ENVISAT-ASAR satellite at 01:26 UTC on 17 October and calculated dominant propagation direction of the typhoon-induced swells (Figure 9).

investigate the dominant propagation directions of the ocean swells induced by Megi and the source regions of the observed microseisms.

3. Detection of the Microseisms Generated by Typhoon Megi

The temporal frequency spectrogram effectively reveals the microseismic signals generated by typhoon Megi at all the seismic stations, with little contamination from occasional large-amplitude transients such as earthquakes, instrumental irregularities, and nonstationary noises. Figure 2a shows the spectrogram at station TWGB located in SE Taiwan; the seismic signal from an M_w 6.7 earthquake in the Gulf of California on 21 October appeared only as short pulses on the spectrogram.

The spectrum analysis shows temporal evolution of the microseisms during the course of typhoon Megi (Figure 2), revealing a rapid intensification with a well-defined typhoon eye at 00:00 UTC, 15 October. Before 06:00 UTC, 17 October when the typhoon center was still over the deep Philippine Sea (Figure 1), only weak SPDF microseisms (S_0, Figure 2a) were detected in the frequency range of 0.21–0.26 Hz. This observation is consistent with the theoretical model of Longuet-Higgins (1950), suggesting that DF microseisms could be generated by depth-independent water pressure fluctuations beneath standing ocean waves in deep sea, but SF microseisms could not be excited directly because the pressure fluctuations from progressive ocean waves decay exponentially with depth. When Megi approached the eastern coastlines of the Luzon Island on 17–18 October, the LPDF (L_1, Figure 2a) and SF microseisms (sf_1, Figure 2a) were detected synchronously, with dominant frequencies increasing nearly linearly from 0.12 to 0.20 Hz and 0.06 to 0.11 Hz, respectively. Simultaneously, the SPDF microseisms (S_1, Figure 2a) were strengthened as the wind speed gradually increased to the maximum. While passing over the Luzon Island, Megi was weakened due to land interaction and its eye became filled and ragged, which significantly reduced the power of the DF microseisms on

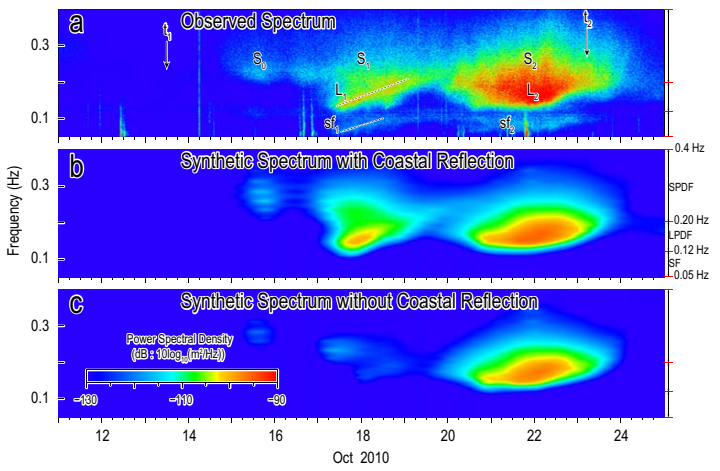

Figure 2. Temporal frequency spectrum of the microseisms generated during the life span of typhoon Megi at station TWGB (121.08°E, 22.818°N, Figure 1). (a) The spectrum of the observed microseisms. t_1 and t_2 denote the initiation and landfall of the typhoon, respectively. (b, c) The spectra of the synthetic microseisms at station TWGB (b) with and (c) without shoreline reflection considered in modeling. Single frequency (SF, sf_1 and sf_2), long-period double frequency (LPDF, L_1 and L_2), and short-period double frequency (SPDF, S_0, S_1, and S_2) microseisms are labeled. The unit (dB) corresponds to $10 \cdot \log_{10}(m^2/Hz)$.

19 October. After Megi began to shift northward to the Taiwan Strait on late 19 October, and especially after it reached the continental shelf on 21 October, the LPDF (L_2) and SPDF (S_2), as well as the SF microseisms (sf_2), were significantly enhanced (Figure 2a).

Although the characteristics of microseisms could vary due to many factors, such as the distance from a recording station to the source regions, the ocean wave field, station site effects, and local noise sources, the evolution of microseismic intensity at all the stations generally shares similar intensity-time behavior. Figure 3 shows the spatially averaged intensity of microseisms from all the stations at different frequency bands. For each station, the intensity was calculated by the integral of the Fourier transformed amplitudes over different frequency intervals, corresponding to the SF, LPDF, and SPDF microseisms, respectively. As expected, the averaged intensities at all the frequency bands were strengthened significantly during the life span of Megi. Interestingly, the LPDF microseisms show a greater dynamic range than the SF and SPDF microseisms, and were strengthened more sharply after 19 October when Megi moved into the SCS.

4. Excitation Regions of the Microseisms

4.1. Constraints From Spatial and Temporal Characteristics of the Microseisms

We explored the spatial distribution of the generated microseismic intensity by typhoon Megi at different frequency bands. Figure 4 shows the intensity images at four representative time points indicated in Figure 3, when typhoon Megi was over the Philippine Sea at 12:00 UTC of 17 October (Figures 4a–4c), the SCS at 12:00 UTC of 19 October (Figures 4d–4f), the continental shelf at 06:00 UTC of 21 October (Figures 4g–4i) and near coastal regions at 00:00 UTC of 23 October (Figures 4j–4l), respectively. In order to investigate the relationship between the microseismic signals and ocean wave field, the wind waves and swells heights were superimposed, using data from the European Centre for Medium-Range Weather Forecasts (ECMWF).

The coastal stations generally recorded stronger microseisms than inland stations and were affected more strongly by local ocean wave field (Figure 4), indicating that at least a significant portion of the microseisms decayed from the coastal areas. This inference of importance of coastal source regions is in good agreement with the temporal evolution of the SF and LPDF microseisms in Figure 2a. The SF microseisms are believed to originate from direct interaction of ocean swells with shallow seafloor or the shore (Hasselmann, 1963). The simultaneous observation of sf_1 and L_1 and the synchronous increasing in their dominant frequency with time (Figure 2a) point to the near-shore origin of both these signals. Therefore, the LPDF microseisms L_1 are expected to originate near the local coasts along the SE Taiwan through the interaction of the reflected ocean waves from the coasts with subsequent incident ocean waves. Furthermore, due to the dispersion effect of ocean waves, the low-frequency components of the ocean waves traveled faster and reached the coasts earlier than the high-frequency components, resulting in corresponding dispersion phenomena in sf_1 and L_1.

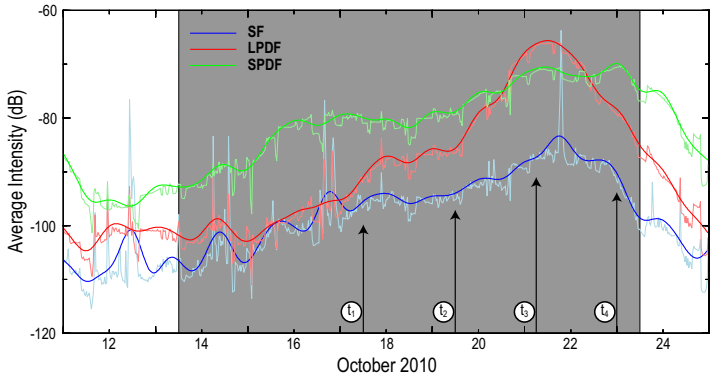

Figure 3. Spatially averaged intensity of microseisms in different frequency bands. The thin lines colored with light blue, red, and green indicate the intensities of SF, LPDF, and SPDF microseisms, respectively, while the thick lines with darker colors represent the corresponding temporal-smoothed lines. The gray shading indicates the life span of typhoon Megi. The black arrows indicate time points, for which the spatial distribution of the microseismic intensity is shown in Figure 4.

Furthermore, we applied linear regression analysis and calculated the correlation coefficient CC_{LPDF} and CC_{SPDF} between the LPDF and SPDF microseismic intensities at different stations and the station-to-typhoon center distances after Megi entered the SCS, respectively (Figure 5). After removing the outliers, which could have been caused by the abnormal response of the seismic stations due to the instrumental failures or incomplete response information (e.g., Yang & Ritzwoller, 2008;

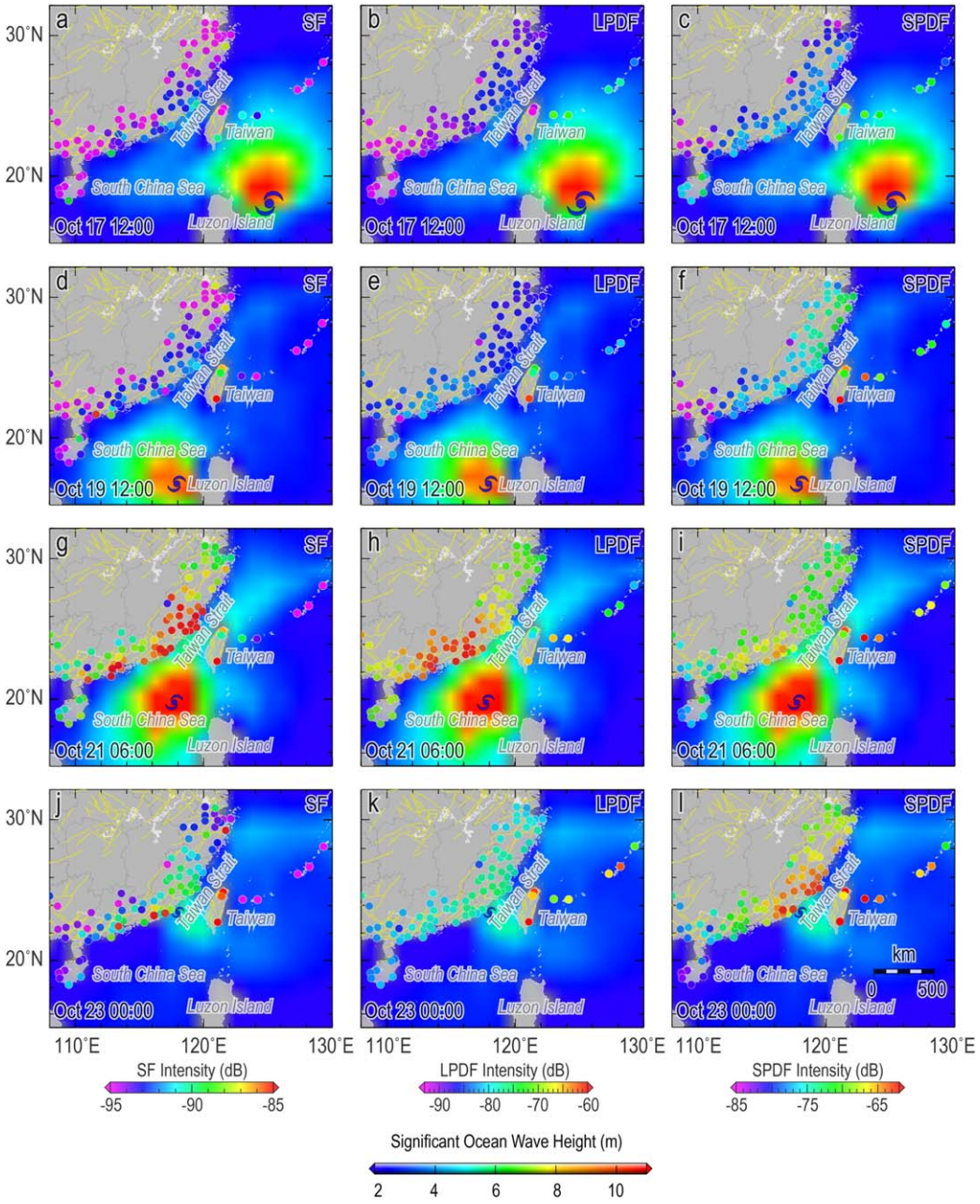

Figure 4. Spatial distribution of the intensity of SF, LPDF, and SPDF microseisms recorded at seismic stations at the time points indicated in Figure 3. The rounded dots indicate the position of seismic stations, with color scaled by microseismic intensity. The significant ocean wave height data were taken from ECMWF, and the blue hurricane symbols indicate the location of the typhoon center.

Zhou et al., 2012), the value of CC_{LPDF} is 0.8656 at 06:00 UTC of 21 October and 0.7980 at 00:00 UTC of 23 October, respectively (Figures 5a and 5b). The value of CC_{SPDF} is 0.6710 at 06:00 UTC of 21 October and 0.8532 at 00:00 UTC of 23 October, respectively (Figures 5c and 5d). The correlation results indicate that both the LPDF and SPDF microseisms could be generated near the typhoon center. The microseisms might have been excited by the seafloor pressure fluctuations triggered by standing ocean waves, which could be formed by the interaction of the induced ocean waves and the trailing waves with opposite propagating directions (Ardhuin et al., 2011; Bromirski et al., 2005; Sufri et al., 2014; Zhang et al., 2010). This is also consistent with the spatial distribution of the intensity of the SPDF microseisms, showing that the stations closer to the typhoon center generally recorded stronger SPDF microseisms (e.g., Figures 4i and 4l).

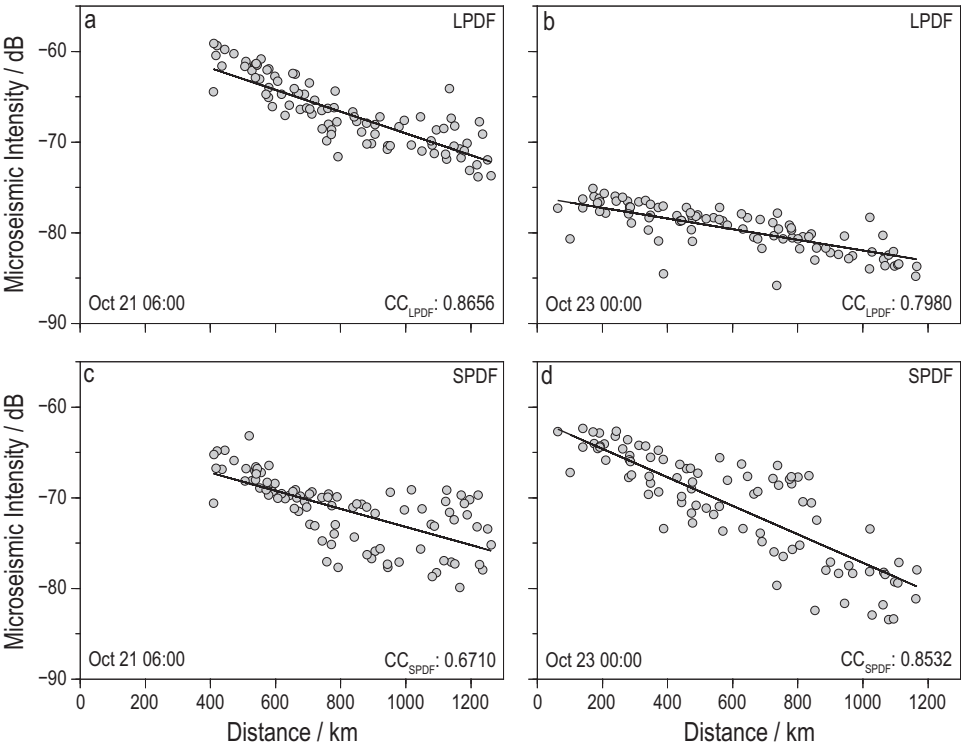

Figure 5. Cross correlation analysis between the intensity of (a, b) LPDF and (c, d) SPDF microseisms and the distance from seismic stations to the typhoon center. CC is the abbreviation for correlation coefficient.

In order to more precisely locate the source region near the typhoon center, we analyzed different types of ocean swells under typhoons according to the studies on the azimuthal sectors with different types of swell using radar altimetry wave observations (Black et al., 2007; Holthuijsen et al., 2012; Wright et al., 2001). For the illustration purpose, a typhoon moving northward in the Northern hemisphere was considered (Figure 6). The winds rotate counter-clockwise around the typhoon center, and reach the highest speed in the NE quadrant near the radius-to-maximum-wind, resulting in the strongest induced ocean waves propagating in the NW direction (Holthuijsen et al., 2012). The strong ocean waves generated at an earlier time t_1 would propagate as young swells and interfere with the ocean waves around the new typhoon center at a later time t_2, resulting in (a) the "following swells" in the NE of the typhoon center, (b) "cross swells" in the NW and SE, and (c) "opposing swells" in the SW corner (Figure 6). The interactions between the forward and backward ocean swells are mostly located in the SW (i.e., left-rear) direction of the typhoon center. Therefore, the source region of microseisms around the typhoon center is probably located in the left-rear corner of the typhoon center, where standing ocean waves could be formed by typhoon-induced ocean waves at different times.

When typhoon Megi was still over the Philippine Sea and approaching the Luzon Island at 12:00 UTC of 17 October (Figure 1), the microseismic signals from Megi were not as strong at the SE China despite that the maximum wind speed exceeding 60 m/s (Figures 4a–4c). One probable reason is that the ocean wave field along the SE China coast was not strengthened since it was far away from Megi and the ocean swells triggered by Megi from the Philippine Sea were sheltered by Taiwan and Luzon Island. In addition, the SPDF microseisms generated near the typhoon center would be highly attenuated during propagating toward the stations in the SE China, because the typhoon center and the stations were located on two different lithospheric plates at that moment. In contrast, the microseisms were strengthened rapidly after Megi moved into the SCS. As Megi moved toward the SE China and approached corresponding stations, the SF and LPDF microseisms generally correlated with the ocean wave height along the coasts (Figures 4d, 4e, 4g, 4h, 4j, and 4k), but the SPDF microseisms were mainly controlled by the station-to-typhoon center distance (Figures 4f, 4i, and 4l).

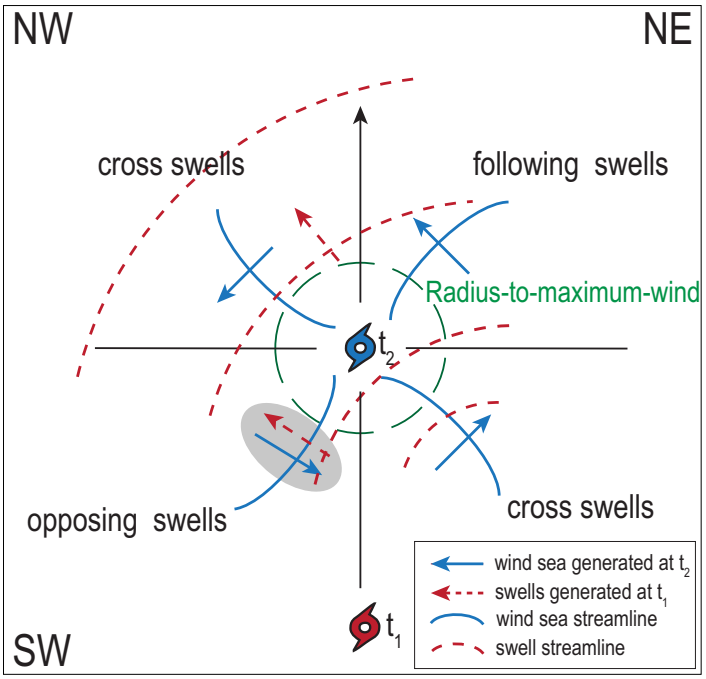

Figure 6. Analysis of the source region around the typhoon center, showing the relationship between the swells generated by the earlier typhoon center and the wind sea generated by the current typhoon center. Red symbol indicates the typhoon center at an earlier time t_1, while blue symbol indicates the typhoon center moving northward in the Northern hemisphere at a later time t_2. The red dashed arrows and curved lines show the propagation directions and streamlines, respectively, of young swells generated at t_1. Blue arrows and curved lines show the propagation directions and streamlines of the locally generated wind sea at t_2. Areas of "following swells," where the young swells and wind sea share the same propagation direction, occur in the NE corner of the typhoon center. Meanwhile, areas of "cross swells," where the young swells and wind sea cross, occur in the NW and SE corners of the typhoon center. Areas of "opposing swells," where the young swells and wind sea have opposite propagation directions, occur in the SW corner of the typhoon center. The gray ellipse in the SW (i.e., left-rear) corner of the typhoon center schematically represents the main source region of microseisms. (Modified from Holthuijsen et al. (2012) with permission from Publisher AGU.)

4.2. Constraints From Synthetic Computation of Microseismic Sources

The DF microseisms are thought to be generated by the standing wave pressure imposed on the seafloor from nonlinear ocean wave-wave interactions (Longuet-Higgins, 1950). We analyzed the spatial distribution of the power spectral density (PSD) of such equivalent surface pressure based on ocean surface gravity waves, using the Ifremer version of the WAVEWATCH-III ocean wave model (Ardhuin & Herbers, 2013; Tolman, 2002). The computed microseismic sources, in the form of frequency spectra at each time point along the ocean surface, have a spatial resolution of 0.5° in longitude and latitude, and a seismic frequency range of 0.082–0.342 Hz. More information on the model settings and analysis procedures can be found in Ardhuin et al. (2011).

Figure 7 shows the spatial distribution of PSD of the calculated equivalent surface pressure at example frequencies of 0.132, 0.160, 0.193, 0.234, and 0.283 Hz and at 12:00 UTC, 17 October (Figures 7a–7j) and 00:00 UTC, 18 October (Figures 7k–7t), respectively. The results are shown for cases with (Figures 7a–7e and 7k–7o) and without (Figures 7f–7j and 7p–7t) coastal reflection considered in the model, respectively. The location of the typhoon center is marked with a crisscross. When the coastal reflection was not considered in the computation, significant wave-wave interaction was observed around the typhoon center at nearly all the example frequencies (Figures 7f–7j and 7p–7t), indicating that both the LPDF and SPDF microseisms could be generated near the typhoon center. However, when the coastal reflection was taken into account, we found that only the wave-wave interaction at the frequency range of 0.132–0.193 Hz was distinctly strengthened near the coasts, and the interaction at the frequencies above 0.2 Hz kept nearly constant.

In order to further quantify the role of coastal reflection in the generation of microseisms, we calculated and compared the mean PSD of the equivalent surface pressure at frequency range of 0.082–0.342 Hz for the cases with and without coastal reflection. Figure 8 shows the mean PSD of the equivalent surface pressure in the ocean area surrounded by the black rectangular box indicated in Figure 7. Through comparing the mean PSD results at 12:00 UTC, 17 October, we found that the wave-wave interaction could be generated largely by coastal reflection at the frequency range of 0.10–0.25 Hz with a peak amplitude around 0.15 Hz (Figure 8a). When Megi moved closer to the Luzon Island and reached its maximum wind speed at 00:00 UTC of 18 October, the wave-to-wave interaction both with and without coastal reflection were strengthened intensively (Figure 8b). However, the wave-to-wave interaction induced by coastal reflection was mainly focused on the frequency band of 0.10–0.20 Hz. We therefore inferred that the SPDF microseisms were mainly generated near the typhoon center, while the LPDF microseisms could be generated both in coastal regions and near the typhoon center.

The synthetic spectra of DF microseisms at station TWGB were also computed with (Figure 2b) and without (Figure 2c) coastal reflection, using the method proposed by Ardhuin et al. (2011). After the equivalent surface pressure was calculated as above and deemed as equivalent source for the vertical ground displacement, the power spectrum of the DF microseisms at any seismic station could be obtained as the instantaneous combination of the sources. During the computation, a vertically symmetric Earth model is applied that neglected all three-dimensional propagation effects and used a uniform quality factor Q for parameterizing seismic wave scattering and dissipation. Comparing with the observed microseisms (Figure 2a), we found that the LPDF microseisms L_1 were well modeled only when coastal reflection was considered (Figure 2b), indicating that the LPDF microseisms L_1 were probably generated in the coastal regions off the

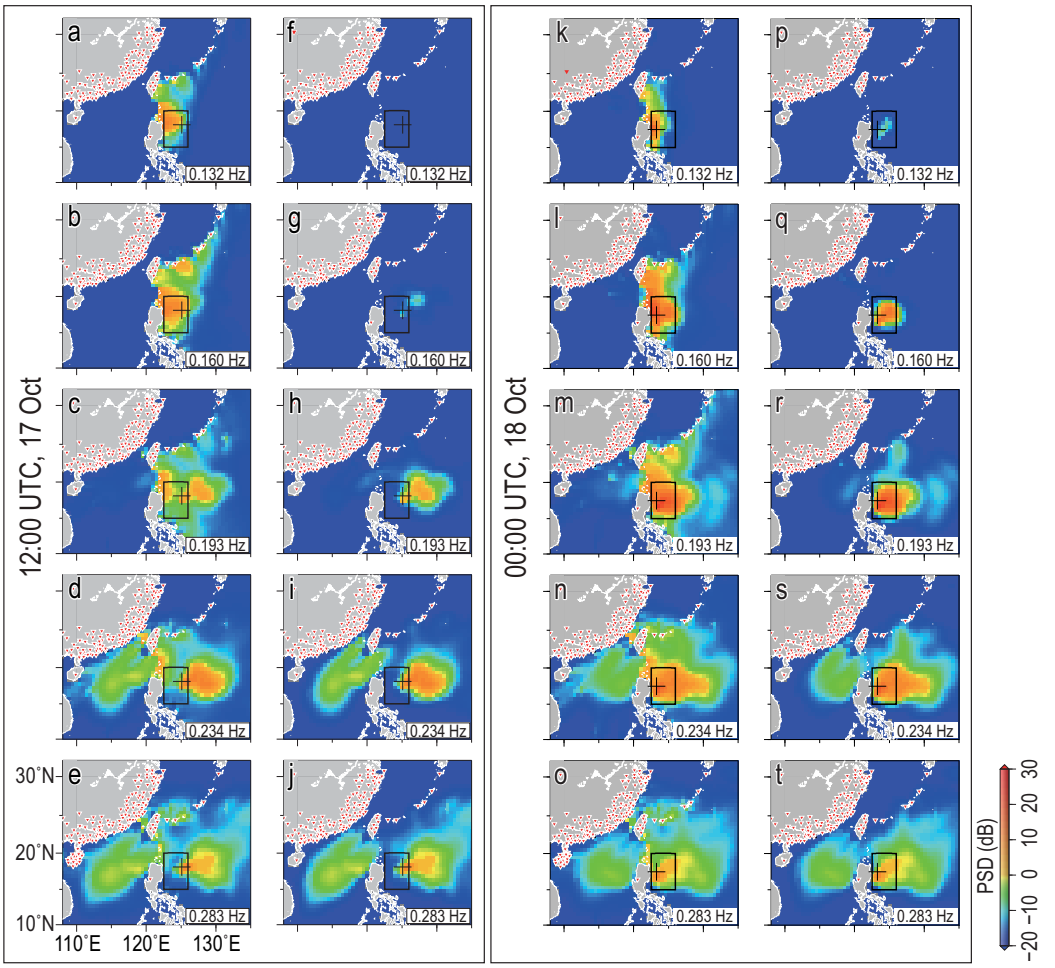

Figure 7. Spatial distribution of the power spectral density (PSD) of the calculated equivalent surface pressure induced by ocean surface gravity waves at five different frequencies at (a–j) 12:00 UTC, 17 October and (k–t) 00:00 UTC, 18 October. Calculation results correspond to cases with (a–e, k–o) and without (f–j, p–t) coastal reflection considered in the WAVEWATCH-III Ifremer model (Ardhuin & Herbers, 2013; Tolman, 2002). The crisscross indicates the location of the typhoon center. The black rectangular box indicates the area for the mean PSD calculation in Figure 8. The unit (dB) here corresponds to $10 \cdot \log_{10}(\mathrm{m}^4/\mathrm{Hz})$.

eastern shorelines of Taiwan, rather than from the source region around the typhoon center over the Philippine Sea. In contrast, the LPDF microseisms L_2 could also be well modeled even when the coastal reflection was not considered (Figure 2c), indicating that the L_2 microseisms were excited by the source near the typhoon center.

Moreover, the above analyses indicate that water depth might be a key factor controlling the generation of DF microseisms near the typhoon center, which is consistent with the interpretation of Tanimoto (2007). The approximation of Longuet-Higgins's (1950) is applicable to shallow water depth less than 1 km, but fails in deep oceans. For this reason, only the LPDF microseisms L_1 generated by coastal source regions were observed when Megi was over the deep Philippine Sea. However, when Megi was over shallow waters after entering the SCS, the LPDF and SPDF microseisms were effectively generated by the source regions near the typhoon center.

4.3. Constraints From Synthetic Aperture Radar Observations

Synthetic aperture radar (SAR) is a space-borne instrument capable of measuring sea surface height with large area coverage and high spatial resolution (Alpers & Bruning, 1986; Hasselmann & Hasselmann, 1991). Figure 9a shows the observed ocean waves during the migration of Megi by C-band ENVISAT-ASAR at 01:26 UTC on 17 October. The observation area coverage is indicated by the dashed rectangular box in Figure 1.

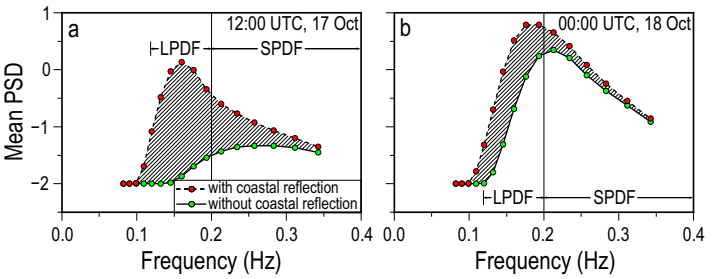

Figure 8. The calculated mean PSD of the equivalent surface pressure in the ocean area surrounded by the black rectangular boxes in Figure 7 at (a) 12:00 UTC, 17 October and (b) 00:00 UTC, 18 October. The dashed lines with red dots and the solid line with green dots correspond to the mean PSD results with and without coastal reflection in modeling, respectively.

We chose three subscenes A–C to investigate the dominant propagation directions of the ocean waves. Figures 9c–9e show the normalized energy density of the three subscenes A–C calculated based on the image colors by using a two-dimensional Fast Fourier Transform (FFT) method. We found that the dominant ocean wave directions, which were also marked with white arrows in Figure 9a, were perpendicular to the wind directions (Figure 9b) derived from ECMWF at 00:00 UTC, indicating that the dominant energy in the subscenes A–C correspond to the ocean swells induced by Megi.

The dominant propagation directions of the ocean swells induced by Megi (Figures 1 and 9) reveal that the ocean swells mainly propagated toward the Ryukyu Islands and Taiwan. This finding further confirmed our above mentioned finding that the observed LPDF microseisms L_1 at station TWGB (Figure 2a) were caused by the typhoon-induced ocean swells at the coastal source regions. In addition, dispersive LPDF microseisms were also observed in the temporal frequency spectra at seismic stations located on the Ryukyu Islands (Figure 10). The generation of such LPDF microseisms, however, depends on the interaction between the coastlines and the incident ocean swells, which are dispersive after long-distance propagation along the ocean surface. Only when the incident ocean swells can be reflected effectively by the coastlines and then interfere with subsequent incoming swells further to form standing ocean waves, the LPDF

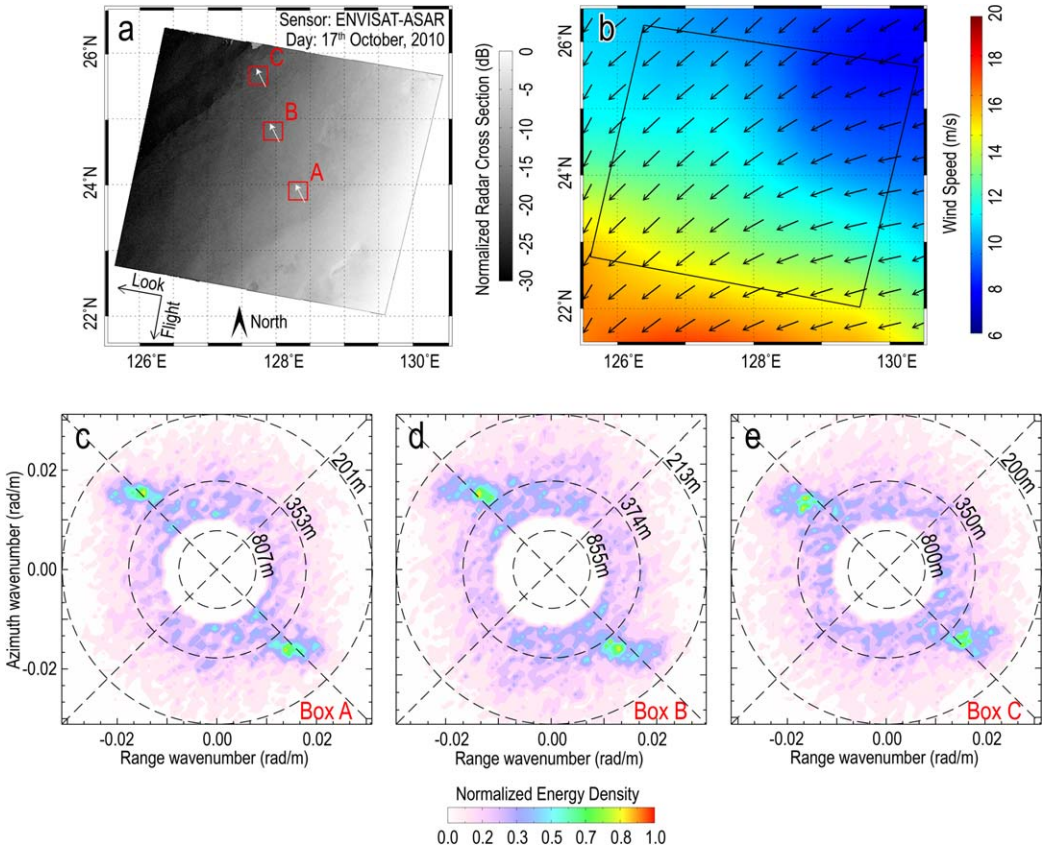

Figure 9. Dominant propagation directions of the ocean swells identified by synthetic aperture radar (SAR). (a) A quick-look image of ENVISAT-ASAR normalized radar cross section acquired at 01:26 UTC, 17 October. (b) The ECMWF wind field direction and speed measured at 00:00 UTC, 17 October. The black rectangular box denotes the coverage of the ENVISAT-ASAR image, which is also shown in Figure 1. (c–e) Two-dimensional SAR spectra corresponding to the selected three subscenes A–C of Figure 9a, respectively. The dominant propagation directions of the ocean swells are labeled with arrows in Figure 9a and Figure 1.

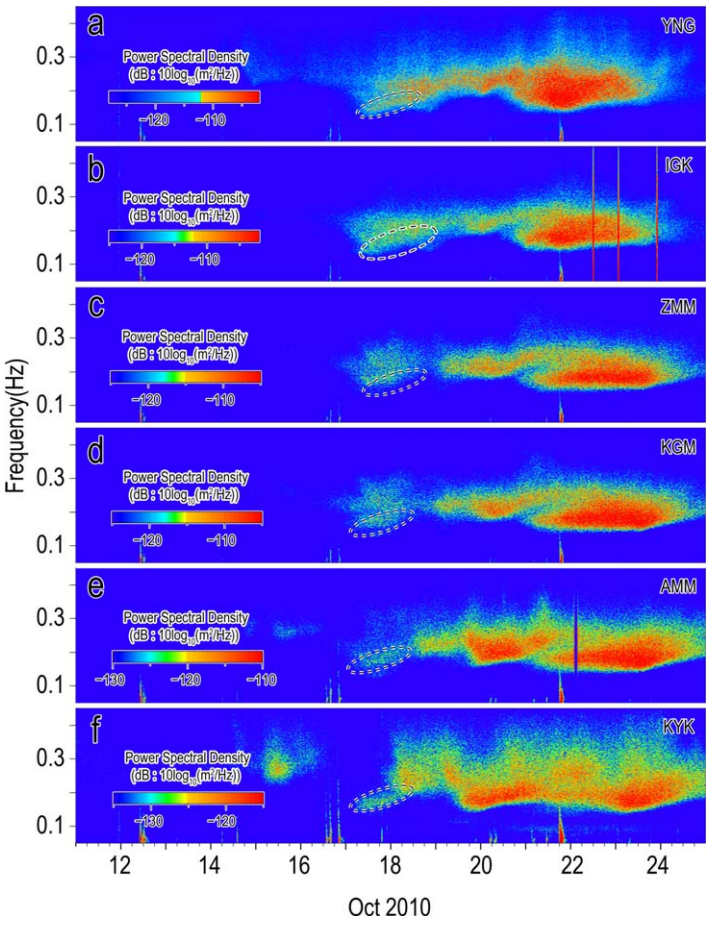

Figure 10. Temporal frequency spectrum of the microseisms generated by typhoon Megi at seismic stations located on the Ryukyu Islands. The dashed ellipses accentuate the dispersive LPDF microseisms generated from coastal source regions. The unit (dB) corresponds to $10 \cdot \log_{10}(m^2/Hz)$.

microseisms could be excited. Consequently, the stations YNG, AMM, and KYK recorded dispersive LPDF microseisms more distinctly against their background noise (Figures 10a, 10e, and 10f), while the dispersive LPDF microseisms were observed relatively weak at stations such as IGK, ZMM, and KGM (Figures 10b–10d).

5. Discussion

Typhoons are known as an energetic source to generate vigorous responses in the ocean and the solid earth beneath, including ocean surface waves higher than 20 m. The recorded seismic noise can be enhanced predominantly in the microseismic frequency band both at the seafloor and on land. The generation mechanisms and source locations of the microseisms generated by typhoons and ocean waves, however, are still under debate. Previous studies suggest that the LPDF and SPDF microseisms have source regions located at shallow water near coastlines and around the typhoon center, respectively (e.g., Bromirski et al., 2005). The new analyses of this study reveal further complexity of the source regions: A source region around the left-rear quadrant of Megi generated both LPDF and SPDF microseisms, while the source near the coastal area mainly generated LPDF microseisms.

Our analyses reveal that Megi generated stronger microseisms when it was over the shallow SCS than the deep Philippine Sea (Figures 2a and 4). We inferred that the water depth has played an important role in the generation of DF microseisms. The effective generation of the DF microseisms by the source near the typhoon center over shallow sea is one of the main reasons for the strengthening of microseisms after Megi traveled into the SCS. The SCS is a marginal sea, and it has extensive continental shelf and long coastlines near the SE China, Taiwan, and the Luzon Island (Figure 1), providing broad coastal source regions for the generation of LPDF microseisms. Furthermore, we noted that the induced ocean waves could directly reach the coastlines of the SE China, Taiwan, and the Luzon Island without much energy attenuation when Megi was over the SCS (Figures 4d–4l). In contrast, when Megi was over the Philippine Sea, most of the induced ocean waves were blocked by Taiwan and the Luzon Island (Figures 4a–4c).

In the last decade, research on seismic noises has become a subject of increasing interests in seismology, following the emergence of noise-based seismic imaging and monitoring applications. The interstation correlations of seismic noise signals have been used to reconstruct Green's function and to invert the Earth's structure (Sabra et al., 2005; Shapiro & Campillo, 2004; Shapiro et al., 2005; Yang & Ritzwoller, 2008; Yao et al., 2006). The accuracy and reliability of such reconstruction depend on the distribution of the seismic noise sources and the assumption that the noise sources are randomized to generate an isotropic and equipartitioned wavefield (Campillo, 2006; Hillers et al., 2012). Therefore, the reconstruction is sensitive to the spatial-temporal property of the seismic noises. In this study, we have investigated the temporal evolution and spatial characteristics of the microseisms induced by Megi, which dominated the spectrogram of the seismic noise field as the strongest component (Figure 2a). We found that the geographically isolated Taiwan Island, being exposed to high-amplitude ocean waves from Megi, has recorded much stronger microseisms compared with the continental SE China (Figure 4). This phenomenon might not be so apparent on the smaller islands, which might lack long-enough coastlines to produce interactions with high-amplitude ocean waves to generate the SF and LPDF microseisms. Taking the station YNG (123.01°E, 24.46°N, Figure 1) as an example, it recorded weaker SF microseisms than most inland stations at 12:00 UTC, 17 October (Figure 4a). In addition, factors such as the source location, phase of the microseism propagation, seismic station site effects, and other local noise sources might also affect the intensity of the observed microseisms.

Typhoons are still difficult to be monitored in real time due to the general lacking of in situ observations under such extreme weather conditions. The causal relationship of the generation of microseisms with the typhoon process and ocean wave field can be potentially used for seismic monitoring of typhoons and ocean swells. A new way of monitoring ocean storms using observations of microseisms has recently emerged (Chen et al., 2015; Chi et al., 2010; Davy et al., 2014; Sufri et al., 2014; Sun et al., 2013). This new approach is expected to provide an effective complement to traditional methods of typhoon monitoring.

Our study revealed that the SPDF microseisms were generated only by the source near the typhoon center. This phenomenon could be potentially used to track typhoon locations using seismological methods. The temporal evolution of the LPDF microseisms excited by the coastal source such as L_1 (Figure 2a) has been found related closely to the dispersion of the typhoon-induced ocean swells, which are so far poorly observed. The group velocity of ocean gravity waves in deep water could be expressed as $U=g/4\pi f$, where g is the gravity acceleration and f is the dominant frequency. Consequently, the dominant frequency f will increase linearly with time (Haubrich et al., 1963), $f(t)=gt/4\pi r$, where r is the distance from the source. Therefore, we could track the origin of the typhoon-induced ocean swells by $r=gt/4\pi f$ (Chevrot et al., 2007), where t/f is the reciprocal of the slope of $f(t)$, offering the possibility of tracking the typhoon center with LPDF microseisms.

6. Conclusions

The temporal and spatial properties of the microseisms generated by the 2010 super typhoon Megi were investigated using seismic waveform data recorded in the SE China, Taiwan, and Ryukyu Islands. We found that the DF microseisms have two main source regions: one was mainly located in the left-rear quadrant of the typhoon center, generating both the LPDF and SPDF microseisms effectively at the shallow sea; while the other one was near the coasts, generating mainly the LPDF microseisms. This interpretation is consistent with synthetic modeling of microseisms using the WAVEWATCH-III Ifremer model, the observed temporal and spatial characteristics of microseisms, and the SAR observations of ocean swells induced by Megi. These findings advance our understanding of the generation mechanisms and source distribution of microseisms, while enhancing the potential of future monitoring typhoons and ocean swells using seismic data.

Acknowledgments
All seismic data were requested from the China Earthquake Networks Center, the IRIS Data Management Center, and the F-net in Japan. The ECMWF reanalysis wind data were accessed at http://www.ecmwf.int. We are grateful to Fabrice Ardhuin for sharing MATLAB code and microseismic source models online. We thank the European Space Agency (ESA) for providing the ENVISAT-ASAR image through AO: C1P13195. A subset of figures were generated using GMT (Wessel & Smith, 1998). The manuscript benefited from thoughtful discussion with Sidao Ni, Fan Zhang, and Zhiyuan Zhou. We also thank three anonymous reviewers of the manuscript for their constructive comments that improved the manuscript. This work was supported by the National Natural Science Foundation of China (grants 41104027, 91628301, U1606401, and 41676044), Natural Science Foundation of Zhejiang Province (LZ14D060001), Opening Fund of SKLGED (SKLGED2013-1-7-E), and Chinese Academy of Sciences (Y4SL021001, Y6YB011001, and QYZDY-SSW-DQC005).

References

Alpers, W., & Bruning, C. (1986). On the relative importance of motion-related contributions to the SAR imaging mechanism of ocean surface waves. *IEEE Transactions on Geoscience and Remote Sensing*, *24*(6), 873–885.

Ardhuin, F., & Herbers, T. H. C. (2013). Noise generation in the solid Earth, oceans and atmosphere, from nonlinear interacting surface gravity waves in finite depth. *Journal of Fluid Mechanics*, *716*, 316–348. https://doi.org/10.1017/jfm.2012.548

Ardhuin, F., Stutzmann, E., Schimmel, M., & Mangeney, A. (2011). Ocean wave sources of seismic noise. *Journal of Geophysical Research*, *116*, C09004. https://doi.org/10.1029/2011JC006952

Black, P. G., D'asaro, E. A., Drennan, W. M., French, J. R., Niiler, P. P., Sanford, T. B.,. . . Zhang, J. A. (2007). Air-sea exchange in hurricanes: Synthesis of observations from the coupled boundary layer air-sea transfer experiment. *Bulletin of the American Meteorological Society*, *88*(3), 357–374. https://doi.org/10.1175/BAMS-88-3-357

Bromirski, P. D. (2001). Vibrations from the "Perfect Storm". *Geochemistry, Geophysics, Geosystems*, *2*(7), 1030. https://doi.org/10.1029/2000GC000119

Bromirski, P. D., Duennebier, F. K., & Stephen, R. A. (2005). Mid-ocean microseisms. *Geochemistry, Geophysics, Geosystems*, *6*, Q04009. https://doi.org/10.1029/2004GC000768

Bromirski, P. D., Stephen, R. A., & Gerstoft, P. (2013). Are deep-ocean-generated surface-wave microseisms observed on land? *Journal of Geophysical Research: Solid Earth*, *118*, 3610–3629. https://doi.org/10.1002/jgrb.50268

Campillo, M. (2006). Phase and correlation in random seismic fields and the reconstruction of the Green function. *Pure and Applied Geophysics*, *163*, 475–502. https://doi.org/10.1007/s00024-005-0032-8

Chen, X., Tian, D., & Wen, L. (2015). Microseismic sources during Hurricane Sandy. *Journal of Geophysical Research: Solid Earth*, *120*, 6386–6403. https://doi.org/10.1002/2015JB012282

Chevrot, S., Sylvander, M., Benahmed, S., Ponsolles, C., Lefevre, J. M., & Paradis, D. (2007). Source locations of secondary microseisms in western Europe: Evidence for both coastal and pelagic sources. *Journal of Geophysical Research*, *112*, B11301. https://doi.org/10.1029/2007JB005059

Chi, W., Chen, W., Kuo, B., & Dolenc, D. (2010). Seismic monitoring of western Pacific typhoons. *Marine Geophysical Research*, *31*(4), 239–251. https://doi.org/10.1007/s11001-010-9105-x

Davy, C., Barruol, G., Fontaine, F. R., Sigloch, K., & Stutzmann, E. (2014). Tracking major storms from microseismic and hydroacoustic observations on the seafloor. *Geophysical Research Letters*, *41*, 8825–8831. https://doi.org/10.1002/2014GL062319

Dorman, L. M., Schreiner, A. E., Bibee, L. D., & Hildebrand, J. A. (1993). Deep-water seafloor array observations of seismo-acoustic noise in the eastern Pacific and comparisons with wind and swell. In B. Kerman (Ed.), *Natural physical sources of underwater sound* (pp. 165–174). New York, NY: Springer.

Friedrich, A., Kruger, F., & Klinge, K. (1998). Ocean generated microseismic noise located with the Grafenberg array. *Journal of Seismology*, *2*(1), 47–64.

Gerstoft, P., Fehler, M. C., & Sabra, K. G. (2006). When Katrina hit California. *Geophysical Research Letters*, *33*, L17308. https://doi.org/10.1029/2006GL027270

Gerstoft, P., Shearer, P. M., Harmon, N., & Zhang, J. (2008). Global P, PP, and PKP wave microseisms observed from distant storms. *Geophysical Research Letters*, *35*, L23306. https://doi.org/10.1029/2008GL036111

Gualtieri, L., Stutzmann, E., Farra, V., Capdeville, Y., Schimmel, M., Ardhuin, F., & Morelli, A. (2014). Modelling the ocean site effect on seismic noise body waves. *Geophysical Journal International*, *197*(2), 1096–1106. https://doi.org/10.1093/gji/ggu042

Hasselmann, K. A. (1963). Statistical analysis of the generation of microseisms. *Reviews of Geophysics*, *1*(2), 177–210. https://doi.org/10.1029/RG001i002p00177

Hasselmann, K., & Hasselmann, S. (1991). On the nonlinear mapping of an ocean wave spectrum into a synthetic aperture radar image spectrum. *Journal of Geophysical Research*, *96*(C6), 10713–10729. https://doi.org/10.1029/91JC00302

Haubrich, R. A., & McCamy, K. (1969). Microseisms: Coastal and pelagic sources. *Reviews of Geophysics*, *7*, 539–571.

Haubrich, R. A., Munk, W. H., & Snodgrass, F. E. (1963). Comparative spectra of microseisms and swell. *Bulletin of the Seismological Society of America*, *53*, 27–37.

Hillers, G., Graham, N., Campillo, M., Kedar, S., Landes, M., & Shapiro, N. (2012). Global oceanic microseism sources as seen by seismic arrays and predicted by wave action models. *Geochemistry, Geophysics, Geosystems*, *13*, Q01021. https://doi.org/10.1029/2011GC003875

Holthuijsen, L. H., Powell, M. D., & Pietrzak, J. D. (2012). Wind and waves in extreme hurricanes. *Journal of Geophysical Research*, *117*, C09003. https://doi.org/10.1029/2012JC007983

Kedar, S., Longuet-Higgins, M., Webb, F., Graham, N., Clayton, R., & Jones, C. (2008). The origin of deep ocean microseisms in the North Atlantic Ocean. *Proceedings of the Royal Society of London, Series A*, *464*, 777–793. https://doi.org/10.1098/rspa.2007.0277

Knudsen, V. O., Alford, R. S., & Emling, J. W. (1948). Underwater ambient noise. *Journal of Marine Research*, *7*, 410–429.

Landès, M., Hubans, F., Shapiro, N. M., Paul, A., & Campillo, M. (2010). Origin of deep ocean microseisms by using teleseismic body waves. *Journal of Geophysical Research*, *115*, B05302. https://doi.org/10.1029/2009JB006918

Lin, J., Lee, T., Hsieh, H., Chen, Y., Lin, Y., Lee, H., & Wen, Y. (2014). A study of microseisms induced by typhoon Nanmadol using ocean-bottom seismometers. *Bulletin of the Seismological Society of America*, *104*(5), 2412–2421. https://doi.org/10.1785/0120130237

Longuet-Higgins, M. S. (1950). A theory of the origin of microseisms. *Proceedings of the Royal Society of London, Series A*, *243*(857), 1–35. https://doi.org/10.1098/rsta.1950.0012

Obrebski, M. J., Ardhuin, F., Stutzmann, E., & Schimmel, M. (2012). How moderate sea states can generate loud seismic noise in the deep ocean? *Geophysical Research Letters*, *39*, L11601. https://doi.org/10.1029/2012GL051896

Rhie, J., & Romanowicz, B. (2004). Excitation of Earth's continuous free oscillations by atmosphere-ocean-seafloor coupling. *Nature*, *431*, 552–556.

Sabra, K. G., Gerstoft, P., Roux, P., Kuperman, W. A., & Fehler, M. C. (2005). Surface wave tomography from microseisms in Southern California. *Geophysical Research Letters*, *32*, L14311. https://doi.org/10.1029/2005GL023155

Schimmel, M., & Gallart, J. (2004). Degree of polarization filter for frequency-dependent signal enhancement through noise suppression. *Bulletin of the Seismological Society of America*, *94*(3), 1016–1035.

Schulte-Pelkum, V., Earle, P. S., & Vernon, F. L. (2004). Strong directivity of ocean-generated seismic noise. *Geochemistry, Geophysics, Geosystems*, *5*, Q03004. https://doi.org/10.1029/2003GC000520

Shapiro, N. M., & Campillo, M. (2004). Emergence of broadband Rayleigh waves from correlations of the ambient seismic noise. *Geophysical Research Letters*, *31*, L07614. https://doi.org/10.1029/2004GL019491

Shapiro, N. M., Campillo, M., Stehly, L., & Ritzwoller, M. H. (2005). High-resolution surface-wave tomography from ambient seismic noise. *Science*, *307*, 1615–1618. https://doi.org/10.1126/science.1108339

Sufri, O., Koper, K. D., Burlacu, R., & de Foy, B. (2014). Microseisms from Superstorm Sandy. *Earth and Planetary Science Letters*, *402*, 324–336. https://doi.org/10.1016/j.epsl.2013.10.015

Sun, T., Xue, M., Le, K., Zhang, Y., & Xu, H. (2013). Signatures of ocean storms on seismic records in South China Sea and East China Sea. *Marine Geophysical Research*, *34*, 431–448. https://doi.org/10.1007/s11001-013-9204-6

Sutton, G. H., & Barstow, N. (1990). Ocean-bottom ultralow-frequency (ULF) seismo-acoustic ambient noise: 0.002 to 0.4 Hz. *Journal of the Acoustical Society of America*, *87*, 2005–2012. https://doi.org/10.1121/1.399328

Tanimoto, T. (2007). Excitation of microseisms. *Geophysical Research Letters*, *34*, L05308. https://doi.org/10.1029/2006GL029046

Tolman, H. L. (2002). *User manual and system documentation of WAVEWATCH-III version 2.22* (NOAA/NWS/NCEP/OMB Tech. Note 222). Silver Spring, MD: NOAA.

Webb, S. C. (1998). Broadband seismology and noise under the ocean. *Reviews of Geophysics*, *36*(1), 105–142.

Wenz, G. W. (1962). Acoustic ambient noise in the ocean: Spectra and sources. *Journal of the Acoustical Society of America*, *34*, 1936–1956.

Wessel, P., & Smith, W. H. F. (1998). New improved version of Generic Mapping Tools released. *Eos, Transactions American Geophysical Union*, *79*, 579.

Wright, C. W., Walsh, E. J., Vandemark, D., Krabill, W. B., Garcia, A. W., Houston, S. H.,. . . Marks, F. D. (2001). Hurricane directional wave spectrum spatial variation in the open ocean. *Journal of Physical Oceanography*, *31*, 2472–2488.

Yang, Y., & Ritzwoller, M. H. (2008). Characteristics of ambient seismic noise as a source for surface wave tomography. *Geochemistry, Geophysics, Geosystems*, *9*, Q02008. https://doi.org/10.1029/2007GC001814

Yao, H., Van der Hilst, R. D., & De Hoop, M. V. (2006). Surface-wave array tomography in SE Tibet from ambient seismic noise and two-station analysis: I—Phase velocity maps. *Geophysical Journal International*, *166*, 732–744. https://doi.org/10.1111/j.1365-246X.2006.03028.x

Zhang, J., Gerstoft, P., & Bromirski, P. D. (2010). Pelagic and coastal sources of P-wave microseisms: Generation under tropical cyclones. *Geophysical Research Letters*, *37*, L15301. https://doi.org/10.1029/2010GL044288

Zhou, L., Xie, J., Shen, W., Zheng, Y., Yang, Y., Shi, H., & Ritzwoller, M. H. (2012). The structure of the crust and uppermost mantle beneath South China from ambient noise and earthquake tomography. *Geophysical Journal International*, *189*, 1565–1583. https://doi.org/10.1111/j.1365-246X.2012.05423.x